JOURNAL OF AIRCRAFT
Vol. 44, No. 6, November–December 2007

Drag Decomposition-Based Adaptive Mesh Refinement

Wataru Yamazaki,* Kisa Matsushima,† and Kazuhiro Nakahashi‡
Tohoku University, Sendai 980-8579, Japan

DOI: 10.2514/1.31064

A new indicator for adaptive mesh refinement is proposed based on a drag decomposition method. The indicator is entropy drag which can be obtained from the drag decomposition postprocessing. The drag decomposition method decomposes total drag into wave, profile, induced, and spurious drag components; the spurious one is due to unphysical entropy production resulting from numerical diffusion and errors. Moreover, the (spurious) entropy drag distribution can be visualized in the flowfield, and thus it is used as the indicator. The newly developed method for adaptive mesh refinement is investigated by inviscid transonic computations for the ONERA M6 wing. The result shows better performance than other mesh refinement methods such as the feature-based method. The authors conclude that the developed adaptive mesh refinement method employing the entropy drag as the indicator is promising for efficient reduction of mesh dependency. The important factors for computational meshes to predict drag accurately are then investigated in detail.

Nomenclature

a	=	sonic speed
Body	=	aircraft surface
C_D	=	drag coefficient
C_L	=	lift coefficient
D	=	drag force
$\boldsymbol{F}_{\text{ind}}$	=	induced drag vector
$\boldsymbol{F}_{(\Delta s,\Delta H)}$	=	entropy and enthalpy drag vector
M	=	Mach number
$\boldsymbol{n} = (n_x, n_y, n_z)$	=	outward unit normal vector to a surface
P	=	pressure
R	=	gas constant
$\mathbf{S}_\infty$	=	closed boundary surface of $\mathbf{V}$
$\boldsymbol{u} = (u_x, u_y, u_z)$	=	velocity vector
$\boldsymbol{u}_\infty = (U_\infty, 0, 0)$	=	freestream velocity vector
$\mathbf{V}$	=	flowfield around the aircraft
V_i	=	control volume of node i
WA	=	wake plane normal to the freestream flow direction
γ	=	specific heat ratio
Δ	=	perturbation term
ΔH	=	stagnation enthalpy variation
Δs	=	entropy variation
$\Delta\boldsymbol{u} = (\Delta u_x, \Delta u_y, \Delta u_z)$	=	perturbation velocity vector
ε	=	indicator for adaptive mesh refinement
μ_l	=	laminar viscosity coefficient
μ_t	=	eddy viscosity coefficient
ρ	=	density
$\vec{\boldsymbol{\tau}} = (\boldsymbol{\tau}_x, \boldsymbol{\tau}_y, \boldsymbol{\tau}_z)^T$	=	stress tensor

Subscripts

∞	=	freestream value
x, y, z	=	orthogonal coordinate system with x axis points in the freestream flow direction

I. Introduction

THE most important parameters for the aerodynamic performance of an aircraft are well known as the lift and drag force in the cruising condition. Recently, owing to advances in numerical schemes and the rapid development of computer technology, computational fluid dynamics (CFD) has achieved significant progress. As is clear from the three meetings of the Drag Prediction Workshop (DPW) in 2001–2006[§,¶] [1–3], however, accurate drag prediction in CFD is still one of the major challenges and crucial issues in the field of aerospace engineering. The effect of computational mesh dependency has been identified as one of the major bottlenecks.

Among CFD approaches to complex aerodynamic configurations, unstructured mesh approaches have several advantages over structured mesh approaches. They can treat complex geometries with more efficiency and less effort. They also have the great flexibility in adaptive mesh refinement (AMR) so that the total number of mesh points can be minimized efficiently. Therefore, the employment of the adaptive mesh refinement strategy is desirable for efficient and accurate unstructured mesh CFD analysis.

The mesh adaptation approach allows one to reduce numerical errors with a limited number of mesh points. The most crucial concern for the adaptive mesh refinement is the selection of the refinement indicator for minimizing the error. A conventional error indicator for the adaptive mesh refinement is the gradient or curvature of flow variables such as pressure, temperature, and so on. However, the engineering interests for the flow analysis are usually global integral outputs such as the lift and/or drag rather than the local flow errors. In general, the local errors related to the gradient/curvature of flow variables are not directly linked to the integral outputs. And so the adaptive mesh refinement using the local flow errors as the indicator does not directly lead one to improve on the accuracy of the lift/drag prediction. Recently, an error estimation method for global functional outputs has been developed using an adjoint sensitivity analysis [4–7] and is being watched with keen interest. The local error amount corresponding to the inaccuracy of the global functional outputs can be predicted and is used as the indicator in this state-of-the-art approach. Although it has been demonstrated that this indicator provides better performance than

Received 21 March 2007; revision received 9 June 2007; accepted for publication 17 June 2007.

*Ph.D. Student, Department of Aerospace Engineering; currently Postdoctoral Researcher, DAAP, ONERA. Student Member AIAA.

†Associate Professor, Department of Aerospace Engineering. Senior Member AIAA.

‡Professor, Department of Aerospace Engineering. Associate Fellow AIAA.

§Data available online at http://aaac.larc.nasa.gov/tsab/cfdlarc/aiaa-dpw/Workshop2/ [retrieved 21 March 2007].

¶Data available online at http://aaac.larc.nasa.gov/tsab/cfdlarc/aiaa-dpw/ [retrieved 21 March 2007].

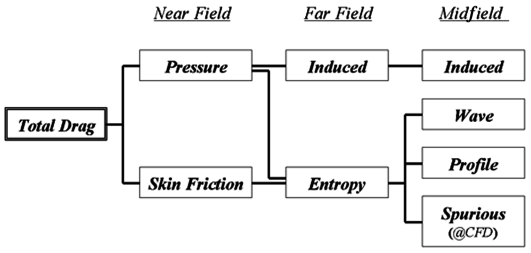

Fig. 1 Drag components and classification.

traditional indicators, it requires additional procedures such as the adjoint analysis, generation of an extra fine mesh, interpolation of flow/adjoint variables from the coarse (present) mesh to the extra fine mesh, one-step CFD computations on the extra fine mesh, and so on. Therefore, this approach has a large computational cost for the evaluation of the indicator.

In the meantime, the midfield drag decomposition method [2,8–12] is also being watched with keen interest recently for more accurate drag prediction. By using this method, total drag can be decomposed into the three physical components of wave, profile, and induced drag, and one spurious drag component as shown in Fig. 1. The spurious drag is based on the effect of spurious entropy production due to numerical diffusion. By excluding the spurious drag component, more accurate drag prediction can be achieved. Moreover, the drag decomposition method has the ability to predict the local drag amount on each node point. As this (spurious) entropy drag amount can be predicted with low computational cost, it is promising as a new indicator for the adaptive mesh refinement.

In this research, therefore, a new indicator is proposed based on the drag decomposition method to reduce the mesh dependency efficiently and to predict drag accurately with a smaller number of mesh points. The newly developed adaptive mesh refinement method is investigated by unstructured mesh inviscid computations for the ONERA M6 wing. In addition, the objectives of this research are not only to demonstrate the advantages of a new indicator, but also to investigate the important factors of computational meshes that can predict drag accurately.

II. Drag Decomposition Method

This section outlines the concept and computational method of the midfield drag prediction method.

A. Near-Field Method

Traditionally, the surface integration of the pressure and stress tensor on the body surface of the aircraft is used for drag prediction in CFD computations. In this method (we call it the near-field method), the drag force is computed as follows:

$$D = \iint_{\text{Body}} [-(P - P_\infty)n_x + \boldsymbol{\tau}_x \cdot \boldsymbol{n}]\,\mathrm{d}s \tag{1}$$

The integral area "Body" indicates the surface of the aircraft. The first term corresponds to the pressure drag component and the second term to the skin friction drag component.

B. Far-Field Method (Wake Integration)

In the drag prediction method based on the theory of conservation of momentum, the drag force is computed as follows:

$$D = \iint_{\mathbf{S}_\infty} [-\rho(u_x - U_\infty)(\boldsymbol{u}\cdot\boldsymbol{n}) - (P - P_\infty)n_x + \boldsymbol{\tau}_x \cdot \boldsymbol{n}]\,\mathrm{d}s \tag{2}$$

The integral area $\mathbf{S}_\infty$ indicates an arbitrary closed surface around the aircraft. It has been demonstrated that Eq. (2) can be transformed as follows by using the small perturbation approximation [8] (subsonic or transonic flow is assumed here):

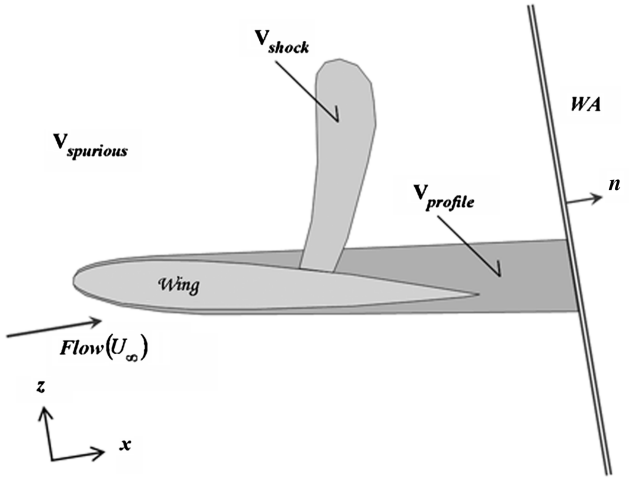

Fig. 2 Schematic sketch for far- and midfield methods.

$$\begin{aligned} D &= \iint_{WA} P_\infty \frac{\Delta s}{R}\,\mathrm{d}s - \iint_{WA} \rho_\infty \Delta H\,\mathrm{d}s \\ &\quad + \iint_{WA} (\boldsymbol{F}_{\text{ind}} \cdot \boldsymbol{n})\,\mathrm{d}s + O(\Delta^2) \\ \boldsymbol{F}_{\text{ind}} &= \left(\frac{\rho_\infty}{2}\left[\left(\Delta u_y^2 + \Delta u_z^2\right) - \left(1 - M_\infty^2\right)\Delta u_x^2\right], \right. \\ &\quad \left. -\rho_\infty \Delta u_y \Delta u_x, \quad -\rho_\infty \Delta u_z \Delta u_x, \right) \end{aligned} \tag{3}$$

The integral area WA indicates a wake plane normal to the freestream flow direction, as shown schematically in Fig. 2. The first term of Eq. (3) corresponds to entropy drag which includes the wave, profile, and spurious drag components. The second term including ΔH can be neglected in cases where external work is not supplied in the flow. The third term including $\boldsymbol{F}_{\text{ind}}$ originates in the vorticity, which corresponds to the induced drag.

C. Midfield Method (Flowfield Integration)

The midfield method is derived from the far-field method by applying the divergence theorem, also known as Gauss's theorem. First, the concept is explained using the entropy and enthalpy term. By using the divergence theorem, the entropy and enthalpy term of the far-field method can be transformed as follows:

$$\begin{aligned} D_{(\Delta s,\Delta H)} &= \iint_{WA} \boldsymbol{F}_{(\Delta s,\Delta H)} \cdot \boldsymbol{n}\,\mathrm{d}s \\ &\cong \iint_{\mathbf{S}_\infty} \boldsymbol{F}_{(\Delta s,\Delta H)} \cdot \boldsymbol{n}\,\mathrm{d}s = \iiint_{\mathbf{V}} \nabla \cdot \boldsymbol{F}_{(\Delta s,\Delta H)}\,\mathrm{d}v \end{aligned} \tag{4}$$

where $\mathbf{V}$ indicates the flowfield around the aircraft, and thus $\mathbf{S}_\infty$ indicates the closed boundary surface of $\mathbf{V}$. In other words, $\mathbf{S}_\infty$ consists of the wake plane of WA and the infinity far-field surfaces of the upstream/lateral regions $\mathbf{S}_{\text{far}}$ as shown schematically in Fig. 3. $\boldsymbol{F}_{(\Delta s,\Delta H)}$ is the entropy and enthalpy drag vector, which is defined in [9] as follows:

$$\begin{aligned} \boldsymbol{F}_{(\Delta s,\Delta H)} &= -\rho \Delta \bar{u} \boldsymbol{u} \\ \Delta \bar{u} &= U_\infty \sqrt{1 + \frac{2\Delta H}{U_\infty^2} - \frac{2[e^{(\gamma-1/\gamma)(\Delta s/R)} - 1]}{(\gamma-1)M_\infty^2}} - U_\infty \end{aligned} \tag{5}$$

$\Delta\bar{u}$ of Eq. (5) can be expanded as a Taylor's series as follows:

$$\begin{aligned} \Delta\bar{u}/U_\infty &= f_{s1}(\Delta s/R) + f_{s2}(\Delta s/R)^2 + f_{H1}\left(\Delta H/U_\infty^2\right) \\ &\quad + f_{H2}\left(\Delta H/U_\infty^2\right)^2 + f_{sH2}(\Delta s/R)\left(\Delta H/U_\infty^2\right) + O(\Delta^3) \end{aligned} \tag{6}$$

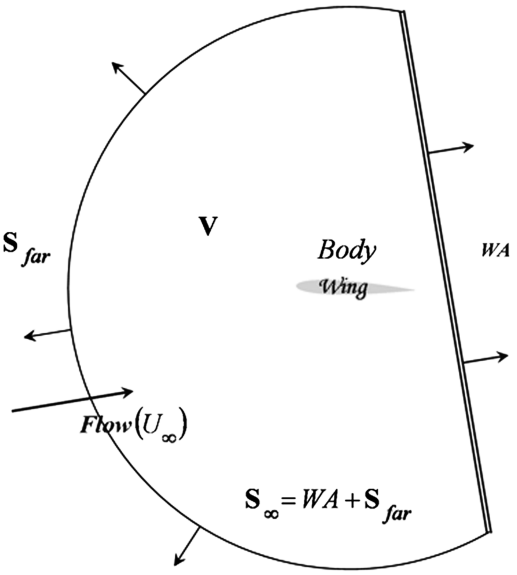

Fig. 3 Relationship between S_∞ and *WA*.

Here

$$f_{s1} = -\frac{1}{\gamma M_\infty^2}, \qquad f_{s2} = -\frac{1+(\gamma-1)M_\infty^2}{2\gamma^2 M_\infty^4}, \ldots \tag{7}$$

Now, calculate the first-order term of entropy variation as follows:

$$\boldsymbol{F}_{\Delta s1} = \frac{U_\infty}{\gamma M_\infty^2}\frac{\Delta s}{R}\rho \boldsymbol{u} \tag{8}$$

Equation (8) is the well-known Oswatitsch formula itself. Moreover, using the small perturbation approximation, Eq. (8) can be rewritten as follows:

$$\boldsymbol{F}_{\Delta s1} = \frac{P_\infty}{\rho_\infty U_\infty}\frac{\Delta s}{R}(\rho_\infty + \Delta\rho)(\boldsymbol{u}_\infty + \Delta \boldsymbol{u}) \tag{9}$$

Here, the formulation $a_\infty^2 = \gamma P_\infty/\rho_\infty$ was also used. Combining Eq. (4) with Eq. (9), the first-order term of entropy drag can be rewritten as follows:

$$\begin{aligned} D_{\text{Entropy}} &= \iint_{WA} \frac{P_\infty}{\rho_\infty U_\infty}\frac{\Delta s}{R}(\rho_\infty + \Delta\rho)(\boldsymbol{u}_\infty + \Delta\boldsymbol{u})\boldsymbol{n}\,\mathrm{d}s \\ &\cong \iint_{WA} P_\infty \frac{\Delta s}{R}\,\mathrm{d}s \end{aligned} \tag{10}$$

Equation (10) is itself the first term of Eq. (3).

Owing to the transformation to the volume integral form, further drag decomposition of the entropy drag term is possible by the domain decomposition of the flowfield **V**. Physically, entropy variation in the flowfield should originate in the shock ($\mathbf{V}_{\text{shock}}$) and wake/boundary layer region ($\mathbf{V}_{\text{profile}}$), so that the entropy variation in the remaining region ($\mathbf{V}_{\text{spurious}}$) is considered to be an unphysical (spurious) phenomenon. The domain decomposition of the flowfield is shown schematically in Fig. 2. Then Eq. (4) can be transformed as follows:

$$\begin{aligned} D_{(\Delta s,\Delta H)} &= \iiint_{\mathbf{V}_{\text{shock}}} \nabla\cdot\boldsymbol{F}_{(\Delta s,\Delta H)}\,\mathrm{d}v + \iiint_{\mathbf{V}_{\text{profile}}} \nabla\cdot\boldsymbol{F}_{(\Delta s,\Delta H)}\,\mathrm{d}v \\ &+ \iiint_{\mathbf{V}_{\text{spurious}}} \nabla\cdot\boldsymbol{F}_{(\Delta s,\Delta H)}\,\mathrm{d}v = D_{\text{wave}} + D_{\text{profile}} + D_{\text{spurious}} \end{aligned} \tag{11}$$

where D_{wave}, D_{profile}, and D_{spurious} correspond to the wave, profile, and spurious drag components, respectively. Moreover, we can evaluate each drag component like a flux computation using the divergence theorem again as follows (only the formula for wave drag is described):

$$D_{\text{wave}} = \iiint_{\mathbf{V}_{\text{shock}}} \nabla\cdot\boldsymbol{F}_{(\Delta s,\Delta H)}\,\mathrm{d}v = \iint_{\mathbf{S}_{\text{shock}}} \boldsymbol{F}_{(\Delta s,\Delta H)}\cdot\boldsymbol{n}\,\mathrm{d}s \tag{12}$$

where $\mathbf{S}_{\text{shock}}$ indicates the boundary surface of $\mathbf{V}_{\text{shock}}$. As the reader can guess, the spurious entropy drag may be generated in the shock and profile region, and the effect cannot be isolated in this approach. However, it is known that the majority of the spurious drag is generated in a region around the leading edge which is outside of the profile (boundary layer) region. And so the spurious drag generated in the shock and profile region is insignificant. The advantages of the midfield method are that it can divide the entropy drag into the wave, profile, and spurious drag components, and it can visualize the drag amount and the generated positions in the flowfield because the integrand of the volume integral form $\nabla\cdot\boldsymbol{F}_{(\Delta s,\Delta H)}$ indicates the entropy drag production rate per unit volume.

The domain decomposition of the flowfield is conducted based on the following shock and profile detective functions. For the detection of the shock region, the following function is used [13]:

$$f_{\text{shock}} = (\boldsymbol{u}\cdot\nabla P)/(a|\nabla P|) \tag{13}$$

For the detection of the wake and boundary layer region, the following function is used [11]:

$$f_{\text{profile}} = (\mu_l + \mu_t)/(\mu_l) \tag{14}$$

The regions which satisfy $f_{\text{shock}} \geq 1$ and $f_{\text{profile}} \geq C_{\text{pro}}\cdot(f_{\text{profile}})_\infty$ are recognized as the upstream region of shock waves and the profile region, respectively. C_{pro} is a cutoff value for selecting the profile region. $C_{\text{pro}} = 1.1$ was recommended from the viewpoint of the robustness [11] and was used in this research.

Likewise, the induced drag can be evaluated as follows:

$$D_{\text{induced}} = \iint_{WA} \boldsymbol{F}_{\text{ind}}\cdot\boldsymbol{n}\,\mathrm{d}s \cong \iint_{\mathbf{S}_\infty} \boldsymbol{F}_{\text{ind}}\cdot\boldsymbol{n}\,\mathrm{d}s \tag{15}$$

III. Unstructured Mesh Methods

This chapter outlines the unstructured mesh methods used in this research.

A. Flow Evaluation

For the unstructured mesh flow computation, three-dimensional flows were analyzed using the Tohoku University Aerodynamic Simulation (TAS) code [14]. Compressible Euler/Navier–Stokes (NS) equations were solved by a finite-volume cell-vertex scheme. The numerical flux normal to the control volume boundary was computed using the approximate Riemann solver of Harten–-Lax–van Leer–Einfelds–Wada (HLLEW) [15]. The second-order spatial accuracy was achieved by a linear reconstruction of the primitive gas dynamic variables inside the control volume with Venkatakrishnan's limiter [16]. In the viscous diffusion terms, the cross derivative terms were neglected, that is, the thin-layer approximation in all three directions. The lower–upper symmetric Gauss–Seidel (LU-SGS) implicit method for unstructured meshes [17] was used for the time integration. The original Spalart–Allmaras model [18] was adopted to treat turbulent boundary layers, and fully turbulent flow was assumed in the computation.

B. Mesh Refinement Method

The refinement algorithm employed in this study is Rivara's bisection algorithm [5,19–21]. A specified tetrahedron is divided into two "sons" by a bisecting plane passing through the midpoint of its longest edge and through the nodes opposite to this edge. This bisection algorithm divides the maximum angle of the tetrahedron, which allows improvement in the quality of refined cell shapes over their "parent" cell shape. This bisection refinement process for a tetrahedron is illustrated in Fig. 4 schematically. Details of the three-dimensional bisection algorithms can be found in [19].

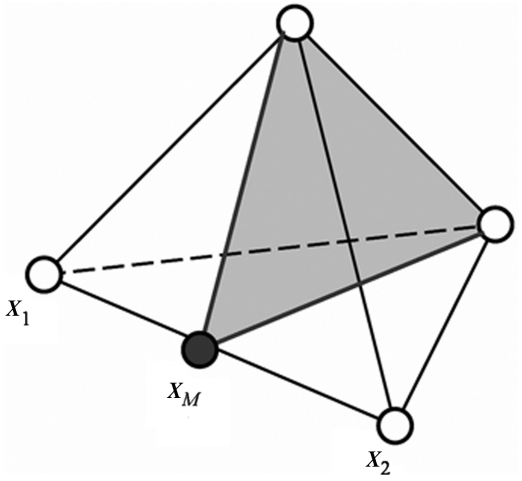

Fig. 4 Schematic sketch for bisection refinement.

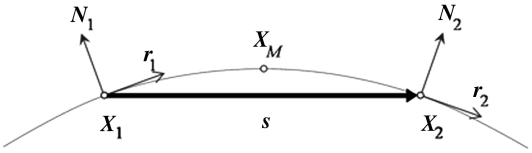

Fig. 5 Schematic sketch for surface recovery.

When a newly added node point is located on the body surface, the new node should be projected onto the smooth surface geometry. In this case, because new nodes are always on the midpoint of the edge, only a quadratic fitting for the edge is required. This can be achieved by the quadratic surface recovery method proposed in [22]. The midpoint location $\boldsymbol{X}_M$ is estimated by using a Hermitian polynomial as follows:

$$\boldsymbol{X}_M = 0.5(\boldsymbol{X}_1 + \boldsymbol{X}_2) + 0.125(\boldsymbol{r}_1 - \boldsymbol{r}_2) \tag{16}$$

where

$$\boldsymbol{r}_i = |\boldsymbol{s}| \cdot \frac{\boldsymbol{N}_i \times (\boldsymbol{s} \times \boldsymbol{N}_i)}{|\boldsymbol{N}_i \times (\boldsymbol{s} \times \boldsymbol{N}_i)|} \qquad (i = 1, 2), \qquad \boldsymbol{s} = \boldsymbol{X}_2 - \boldsymbol{X}_1 \tag{17}$$

$\boldsymbol{X}_1$ and $\boldsymbol{X}_2$ are the location vectors of both ends of the edge, and $\boldsymbol{N}_1$ and $\boldsymbol{N}_2$ are unit normal vectors at each node, as shown in Fig. 5. These normal vectors are computed by summing up the contribution from each surface cell sharing the node. If $\boldsymbol{X}_1$ or $\boldsymbol{X}_2$ is on a ridge such as the trailing edge, the midpoint location may deviate from the initial geometry. To prevent this issue, multiple normal vectors are defined at ridge nodes when the angle between the normal vectors of two adjacent surface cells is larger than a specified degree [5]. This is illustrated in Fig. 6 schematically.

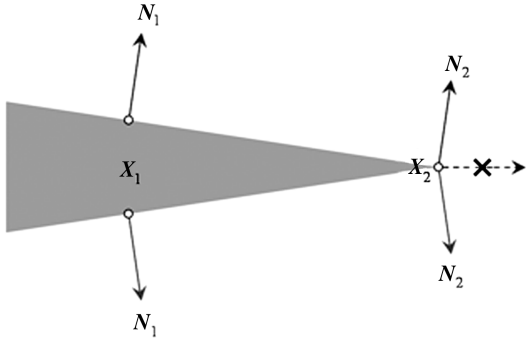

Fig. 6 Special treatment for a sharp ridge.

C. Initial Mesh Generation

The initial coarse mesh around the ONERA-M6 wing configuration has 63,795 nodes and 338,182 tetrahedral elements. The surface mesh was generated by using an advancing front approach [23,24]. The tetrahedral volume mesh was generated by using a Delaunay approach [25]. The distance between the wing and the outer boundary was about 20 times of the root chord length.

IV. Validation of the Drag Decomposition Method

For the validation study of the drag decomposition method, the unstructured mesh computational result of the subject of DPW-2** is analyzed. The drag polar of the DLR-F6 wing-body configuration was computed under the condition of a Mach number of 0.75 and a Reynolds number of 3×10^6. A coarse unstructured mesh, which was provided as one of the official meshes for DPW-2 [26], was used in the computation. The number of mesh points was about 1×10^6.

In Fig. 7, the unstructured mesh with the surface pressure at an angle of attack of 0.49 deg is visualized. The results of drag prediction and decomposition are shown in Fig. 8. In Fig. 8, the experimental data** and the structured mesh results computed by elsA code [2] are also plotted. In this figure, the prefixes NF and MF represent the near-field and midfield drag predictions, respectively. It was confirmed that the wave, profile, and induced drag components showed good agreement with those of elsA. The MF_Pure plot indicates the sum of the physical drag components (wave + profile + induced drag)—in other words, the remainder after subtracting the spurious drag from the total drag. The pure drag showed good agreement with the experimental data while the total drag showed about a 20 drag counts overestimation which was the spurious drag due to the mesh coarseness (1 drag count=

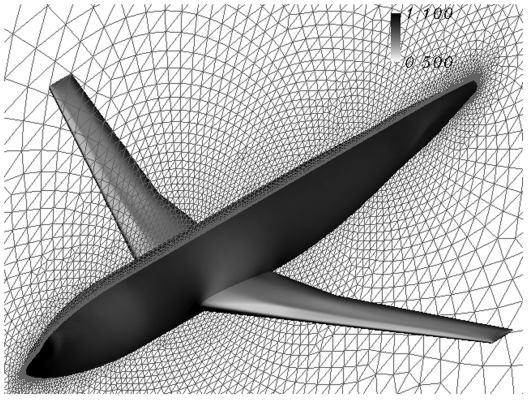

Fig. 7 Mesh and pressure visualization of DLR-F6.

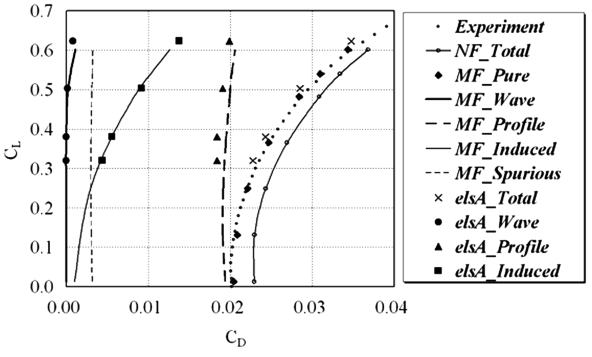

Fig. 8 Drag decomposition results of DLR-F6.

**Data available online at http://aaac.larc.nasa.gov/tsab/cfdlarc/aiaa-dpw/Workshop2/ [retrieved 21 March 2007].

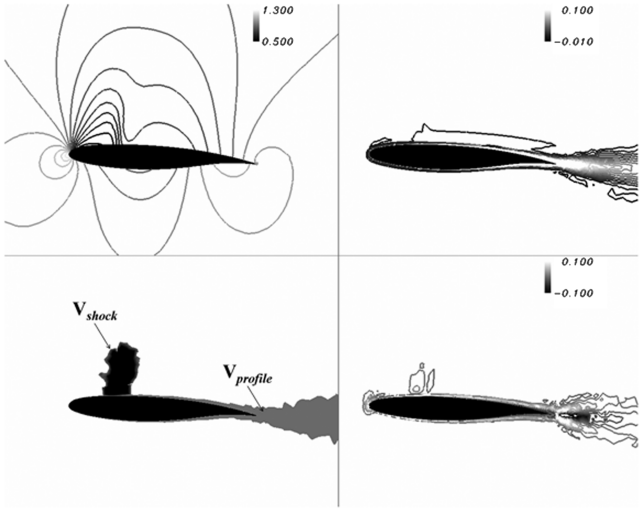

Fig. 9 Flowfield visualization at a 33% semispan section of DLR-F6. Upper/left: pressure; upper/right: entropy variation; lower/left: domain decomposition; lower/right: entropy drag distribution ($\nabla \cdot \boldsymbol{F}_{(\Delta s,\Delta H)}$).

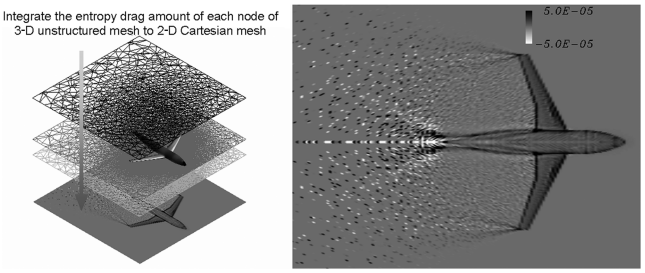

Fig. 10 Entropy drag production map of DLR-F6.

1×10^{-4}). This result showed that more accurate drag prediction could be achieved by using the midfield drag decomposition.

In Fig. 9, the flowfield visualizations at an angle of attack of 0.49 deg, 33% semispan section are shown. The entropy drag generation at the leading/trailing edge, boundary layer, shock positions, and wake region was confirmed. The spurious drag was mainly generated around the leading edge and was caused by the numerical diffusion relating to the mesh coarseness. In Fig. 10, the entropy drag production maps on the x–y plane are shown. To create this figure, first a uniform Cartesian mesh was made on the x–y plane, and then the entropy drag amount of each node of the unstructured mesh was integrated to each cell of the Cartesian mesh referring to the x and y coordinates. The black/white points on the left side indicate the diffusion of the wing-tip vortex and wake. In this way, the drag amount and the generated positions could be predicted and visualized by using the drag decomposition method. Therefore, the authors expected to achieve efficient adaptive mesh refinement by using the entropy drag distribution as the indicator.

V. Indicator of Mesh Adaptation

This section outlines the indicator of adaptive mesh refinement used in this research.

A. Entropy Drag-Based Mesh Adaptation

In the drag decomposition method, the drag components can be predicted by the volume and/or surface integration of entropy, stagnation enthalpy, and vorticity terms around the aircraft, as described in the previous section. The effect of numerical diffusion is mainly included in the entropy drag terms. The formula for the entropy (and enthalpy) drag prediction is as follows:

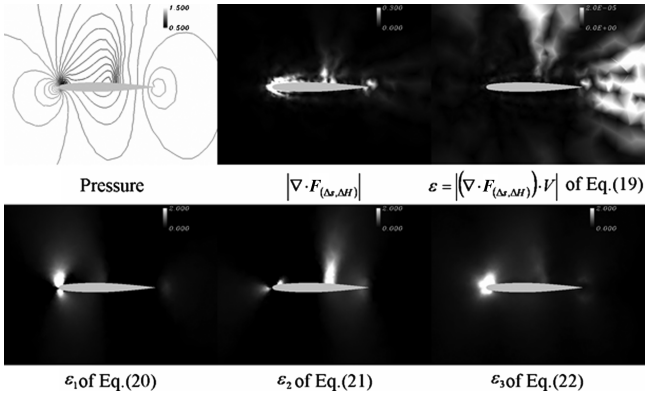

Fig. 11 Distributions of indicators at a 33% semispan of the ONERA M6 wing.

$$D_{(\Delta s,\Delta H)} = \iiint_{\mathrm{V}} \nabla \cdot \boldsymbol{F}_{(\Delta s,\Delta H)}\, \mathrm{d}v = \sum_{\mathrm{node}} [(\nabla \cdot \boldsymbol{F}_{(\Delta s,\Delta H)})_i \cdot V_i] \quad (18)$$

where $(\boldsymbol{F}_{(\Delta s,\Delta H)})_i$ and V_i denote the entropy and enthalpy drag vector and control volume of node i, respectively. This $(\nabla \cdot \boldsymbol{F}_{(\Delta s,\Delta H)})_i$ indicates the entropy drag production rate per unit volume of node i. On the other hand, $(\nabla \cdot \boldsymbol{F}_{(\Delta s,\Delta H)})_i \cdot V_i$ indicates the entropy drag amount of node i. These distributions of the initial mesh of the ONERA M6 wing are illustrated in the upper part of Fig. 11. The distribution of $(\nabla \cdot \boldsymbol{F}_{(\Delta s,\Delta H)})_i$ is concentrated at the leading/trailing edge (spurious drag) and shock position (wave drag). On the other hand, the distribution of $(\nabla \cdot \boldsymbol{F}_{(\Delta s,\Delta H)})_i \cdot V_i$ was spread widely at the upstream region, upper region of shock, wake region, and so on. In this research, the absolute value of the entropy drag amount of each node is selected as the indicator of the adaptive mesh refinement as follows:

$$(\varepsilon)_i = |(\nabla \cdot \boldsymbol{F}_{(\Delta s,\Delta H)})_i \cdot V_i| \quad (19)$$

B. Feature-Based Mesh Adaptation

To compare with the performance of the traditional mesh adaptation method, the feature-based mesh adaptation [7,27] is also executed. In this method, the following three functions are used as the indicators simultaneously:

$$(\varepsilon_1)_i = \max\left[-\frac{\boldsymbol{u}_i}{|\boldsymbol{u}_i|} \cdot \nabla P_i, 0\right] \quad (20)$$

$$(\varepsilon_2)_i = \max\left[+\frac{\boldsymbol{u}_i}{|\boldsymbol{u}_i|} \cdot \nabla P_i, 0\right] \quad (21)$$

$$(\varepsilon_3)_i = \left|\nabla P_i - \frac{\boldsymbol{u}_i}{|\boldsymbol{u}_i|}\left(\frac{\boldsymbol{u}_i}{|\boldsymbol{u}_i|} \cdot \nabla P_i\right)\right| \quad (22)$$

where $\boldsymbol{u}_i$ and P_i indicate the velocity vector and pressure of node i, respectively. ε_1 and ε_2 focus the regions of expansion and compression, respectively. ε_3 represents the magnitude of the gradient normal to the flow direction. In the lower part of Fig. 11, these distributions of the initial mesh of the ONERA M6 wing are also illustrated.

C. Refinement Criterion

The refinement criterion is determined simply as follows. The node i is flagged for refinement when the value of the indicator falls in the following range:

$$(\varepsilon)_i \geq \mu + C \cdot \sigma \quad (23)$$

where μ and σ indicate the mean and standard deviation of the indicator over all the mesh nodes, respectively. C is a relaxation

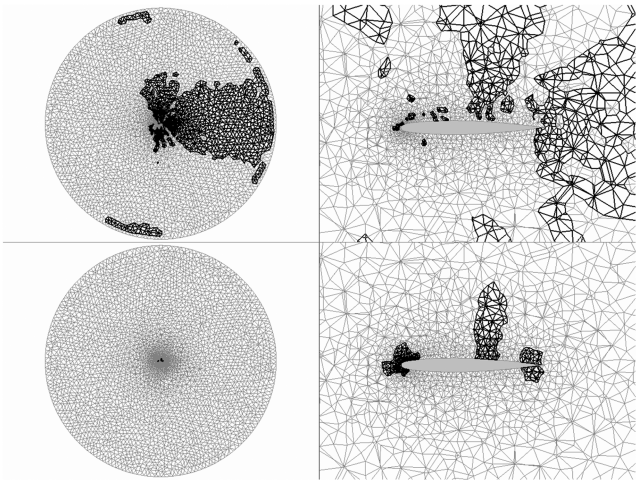

Fig. 12 Refinement regions of initial mesh at a 33% semispan of the ONERA M6 wing. Upper: entropy drag based; lower: feature based.

factor and usually set to 0.0–0.5. For the feature-based mesh adaptation, all three indicators are used simultaneously to capture the particular features in the flowfield. In Fig. 12, the refinement regions of the initial mesh identified by both methods are illustrated.

VI. Results and Discussion

The efficiency of the developed adaptive mesh refinement method was investigated by inviscid transonic computations around the ONERA M6 wing. In this research, the flow conditions were fixed to a Mach number of 0.84 and an angle of attack of 3.06 deg. Starting from the coarse mesh of 63,795 nodes, the entropy drag-based and feature-based mesh refinement procedures were iterated 4 times. The uniform refinement (all nodes were flagged) was also executed for the purpose of comparison. The variation in the pressure drag coefficient (NF_Total) is plotted in Fig. 13. In [5], the mesh converging drag value at the same flow condition was estimated by an extrapolation approach and was about 105–110 drag counts. In [28], a coarse structured mesh result was reported and the pressure drag was about 114 drag counts. So the range of 105–110 drag counts is also indicated in Fig. 13. Our objective was to predict drag accurately with a smaller number of mesh points. The feasible direction in Fig. 13 is also indicated by a gray arrow.

The pressure drag coefficient of the uniform refinement was satisfactorily reduced to the extrapolated range. Although the feature-based refinement showed a better performance than the uniform refinement at the beginning, it finally reached the ceiling and showed a worse performance than the uniform refinement. The newly developed entropy drag-based method showed a sufficient performance. The pure drag predicted by the drag decomposition method is also included in Fig. 13. It showed an excellent performance and almost agreed with the extrapolated value even in the coarse mesh computations. In detail, the pure drag in all cases was distributed within the range of nine counts, while the pressure (near-field total) drag was distributed within the range of 43 counts. This result showed that the physical drag components could be predicted almost independent of the mesh resolution by excluding the effect of unphysical entropy production. In addition, this result supported the effectiveness of the new indicator based on the drag decomposition method.

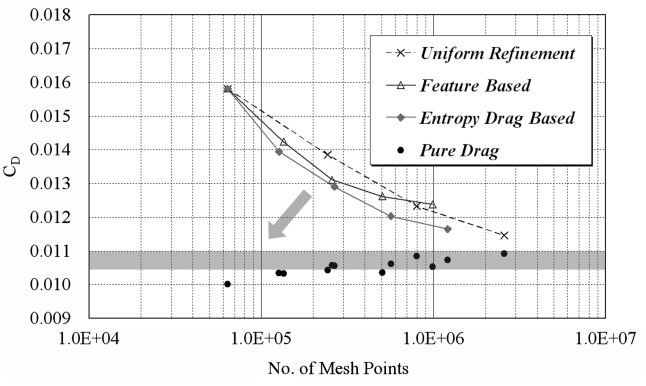

Fig. 13 Inviscid drag prediction for the ONERA M6 wing.

The initial and final refinement meshes' visualizations are compared in Figs. 14 and 15. The flowfield visualizations are compared in Figs. 16–20. It was confirmed that the refinement region specified by the feature-based method was concentrated around the leading edge and shock waves whereas the region specified by the entropy drag-based method was spread, not only around the leading edge and shock, but also around the wake and far-field upstream region. The entropy distribution of the feature-based method was spread widely compared with the distribution of the entropy drag-based method. On the other hand, the entropy distribution of the entropy drag-based method showed good agreement with the distribution of the uniform refinement even though the number of mesh points was about half. The distribution of indicator $(\varepsilon)_i$, in other words, the distribution of the entropy drag amount, showed the excellent performance of the entropy drag-based method directly. In the feature-based method, the (spurious) entropy drag amount was reduced only around the wing and remained in the far-field region. On the other hand, the entropy drag amount was reduced in all regions in the final mesh of the entropy drag-based method.

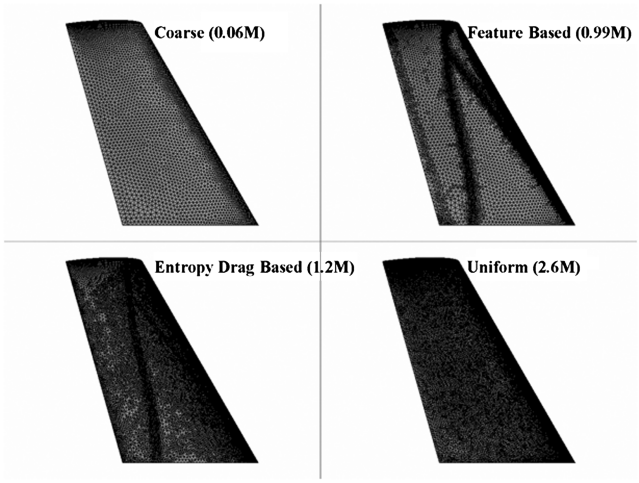

Fig. 14 Upper surface mesh visualization of initial and final refinement meshes of the ONERA M6 wing.

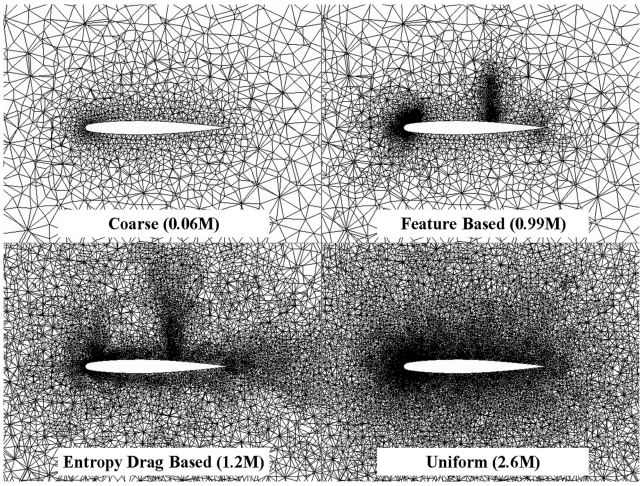

Fig. 15 Volume mesh visualization of initial and final refinement meshes at a 33% semispan of the ONERA M6 wing.

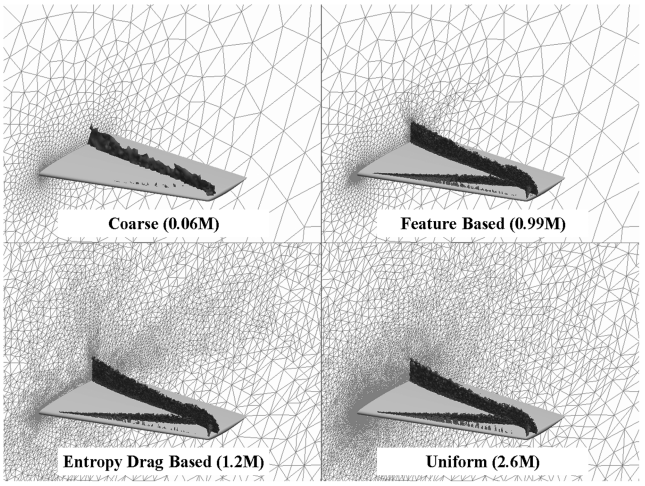

Fig. 16 Shock visualization of initial and final refinement meshes of the ONERA M6 wing.

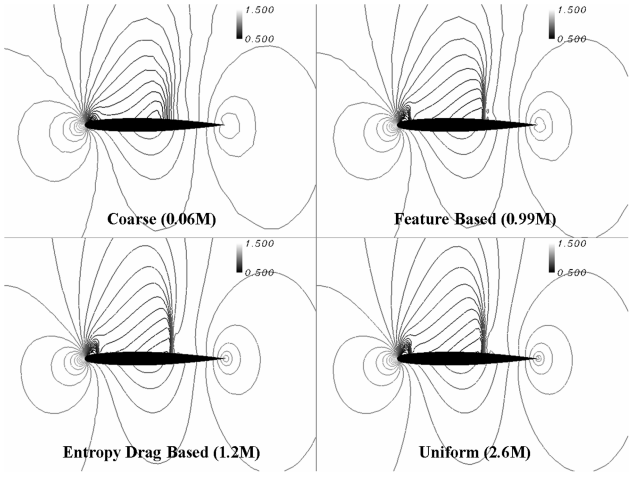

Fig. 17 Pressure distribution of initial and final refinement meshes at a 33% semispan of the ONERA M6 wing.

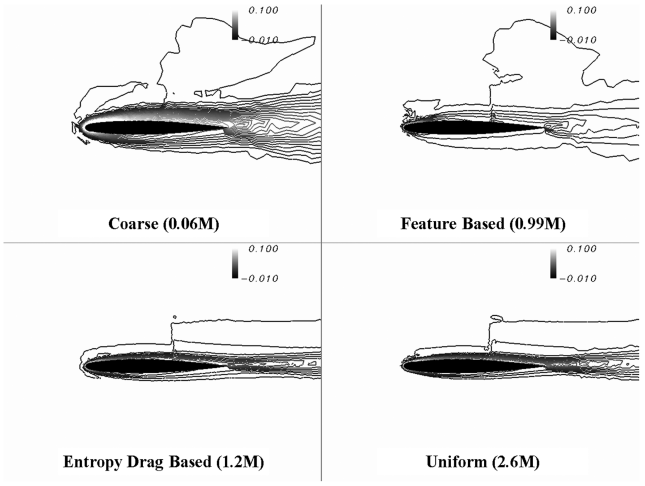

Fig. 18 Entropy variation of initial and final refinement meshes at a 33% semispan of the ONERA M6 wing.

Therefore, the reason for the worse performance of the feature-based method can be explained as follows. At first, the numerical diffusion around the leading edge and shock (near field) was the dominant error in the inaccuracy of drag prediction. Therefore, the feature-based refinement showed a better performance than the uniform refinement at the beginning. With the refinement at the near-field region, however, the far-field numerical diffusion altered as the dominant error, and the feature-based method reached the ceiling. It can be concluded that simple gradient-based refinement methods like the feature-based method may reach a ceiling because they cannot flag the far-field region. This analysis indicated the far-field mesh resolution, in other words, the control of the mesh size transition rate from the near field to the far field is important for computational meshes to predict drag accurately.

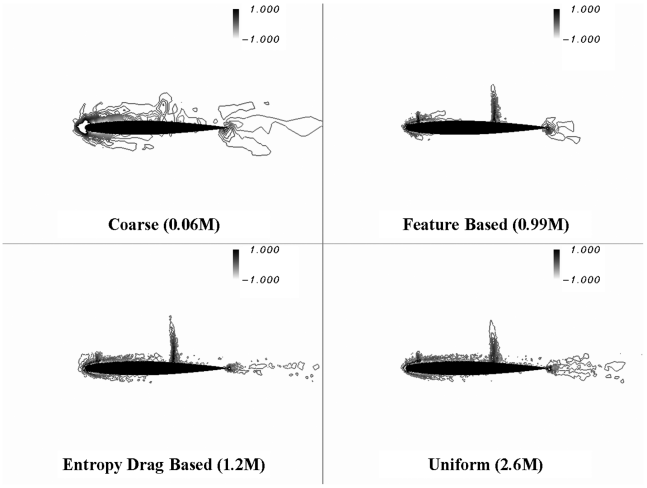

Fig. 19 Entropy drag distribution ($\nabla \cdot F_{(\Delta s, \Delta H)}$) of initial and final refinement meshes at a 33% semispan of the ONERA M6 wing.

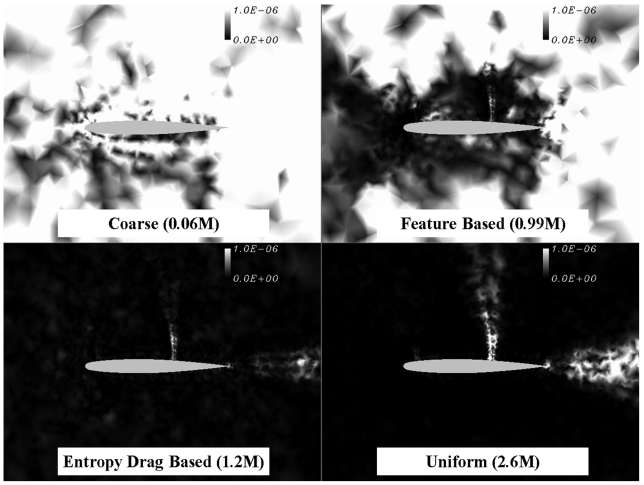

Fig. 20 Entropy drag amount [ε of Eq. (19)] of initial and final refinement meshes at a 33% semispan of the ONERA M6 wing.

To put it briefly, on the other hand, the indicator of the newly developed entropy drag-based method is the product of the entropy gradient and the control volume of each node as understood from Eq. (19). Therefore, it can flag not only the near field, but also the far field because the far field usually has a larger control volume.

The entropy drag production map is illustrated in Fig. 21. It was confirmed in the refinement meshes that the shock waves could be captured sharply and the spurious drag was reduced around the leading/trailing edge. The wake and wing-tip vortex diffusion was reduced sufficiently by the entropy drag-based mesh adaptation. This result showed that the entropy drag-based method was superior, not only in predicting drag accurately, but also in capturing the physical phenomena precisely.

VII. Further Investigation

As shown in Fig. 12, the indicator of the entropy drag-based method specified even the far wake as the refinement region. This is

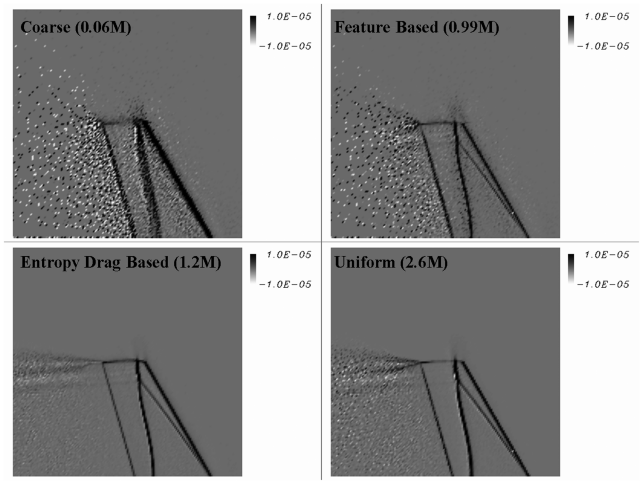

Fig. 21 Entropy drag production map of initial and final refinement meshes of the ONERA M6 wing.

because of the effect of the entropy variation in the wake and by the wing-tip vortex diffusion. It is obvious that the phenomenon in the far wake is only entropy variation (not production) if the effect of the wing-tip vortex diffusion can be neglected. And so the adaptive mesh refinement of the far wake is not important for accurate drag prediction. On the other hand, it was confirmed in the previous section that the mesh resolution at the upstream far-field region had the significance for the accurate drag prediction. Therefore, a modified indicator to reduce the refinement region only for the wake direction is proposed as follows:

$$(\varepsilon_{\mathrm{mod}})_i = \begin{cases} (\varepsilon)_i & (x_i < x_{\mathrm{trail}}) \\ (\varepsilon)_i * e^{\left(-a\frac{x_i - x_{\mathrm{trail}}}{x_{\mathrm{down}} - x_{\mathrm{trail}}}\right)} & (x_i \geq x_{\mathrm{trail}}) \end{cases} \tag{24}$$

where x_i, x_{trail}, and x_{down} are the x coordinates of node i, the trailing edge of the tip position, and the downstream outer boundary, respectively. In cases of wing-body airplane configurations, x_{trail} should be replaced with the x coordinate of the tail of the fuselage. The concept of this modification is only to reduce the strength of the indicator at the far wake. a is the scaling parameter. In Fig. 22, the refinement region specified by the modified indicator is compared with the original one. The specified region in the near field had the same characteristics while the far wake was not specified in the modified indicator. The result of the mesh adaptation is shown in Fig. 23. The modified entropy drag-based refinement showed a better performance than the original one. In Fig. 23, the drag decomposition

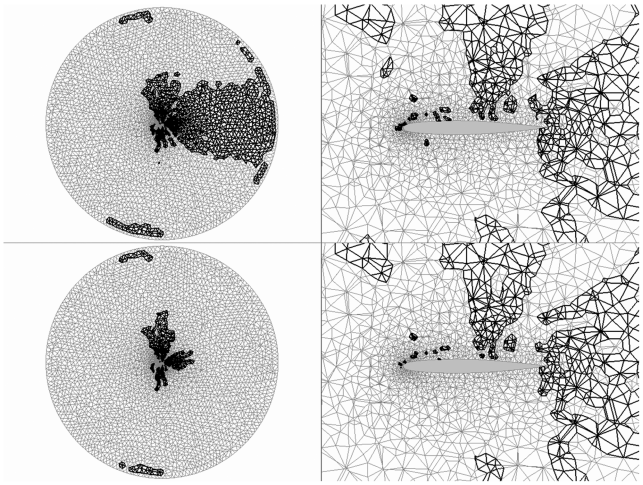

Fig. 22 Refinement regions of initial mesh at a 33% semispan of the ONERA M6 wing. Upper: original entropy drag based; lower: modified one.

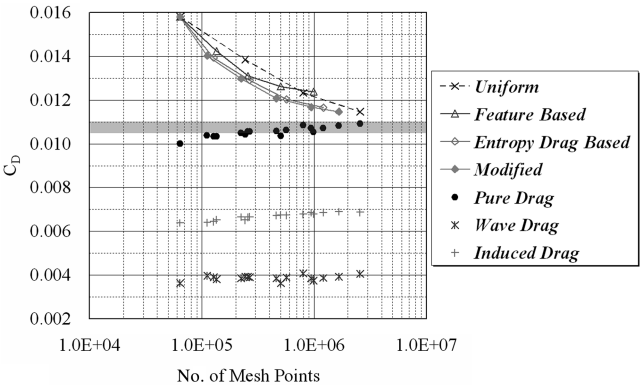

Fig. 23 Further improvement of the entropy drag-based mesh adaptation in the inviscid drag prediction of the ONERA M6 wing.

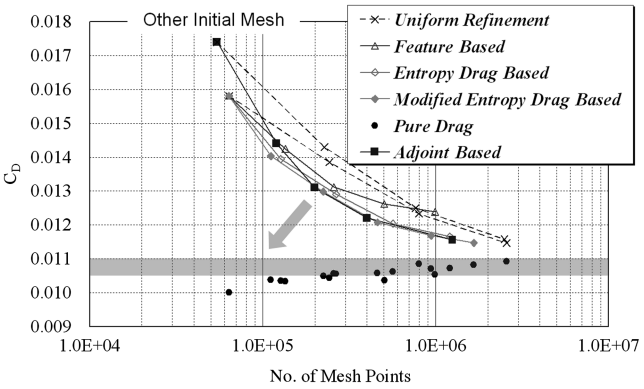

Fig. 24 Comparison with the adjoint-based mesh adaptation in inviscid drag prediction of the ONERA M6 wing.

results for all cases are also included. It was confirmed that the lower pure drag in coarse meshes was due to the lower induced drag. This was because of the lower lift prediction in the coarse meshes.

Moreover, the result of the modified entropy drag-based refinement was compared with that of the state-of-the-art adjoint-based refinement investigated in [5]. This is shown in Figs. 24 and 25. In Fig. 25, the x axis was modified to the grid factor which was defined as follows:

$$\text{grid factor} = (\text{no. of mesh points})^{-2/3} \tag{25}$$

Although the initial coarse mesh of the adjoint-based refinement was different from that used in this research, the tendency toward drag reduction by the adaptive mesh refinement was almost the same as with the entropy drag-based method. The final mesh and the flowfield visualizations are compared in Figs. 26 and 27 in the same manner as

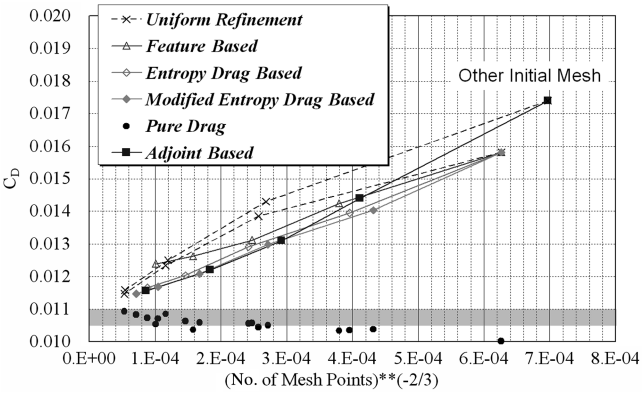

Fig. 25 Comparison with the adjoint-based mesh adaptation in inviscid drag prediction of the ONERA M6 wing by using the grid factor.

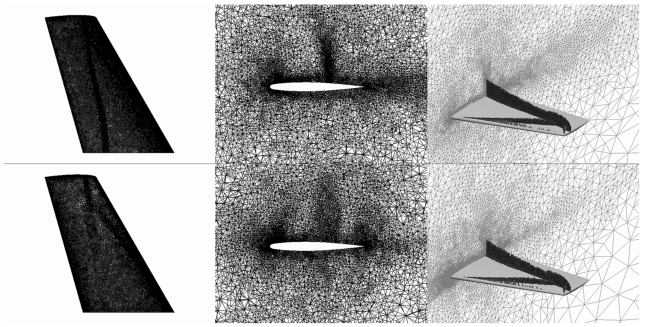

Fig. 26 Comparison of final meshes of the ONERA M6 wing. Upper: modified entropy drag based (1.66×10^6); lower: adjoint based (1.25×10^6) [5].

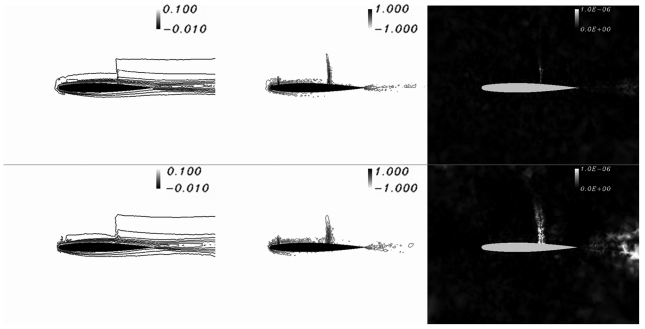

Fig. 27 Comparison of the flowfield of final meshes at a 33% semispan of the ONERA M6 wing. Upper: modified entropy drag based (1.66×10^6); lower: adjoint based (1.25×10^6) [5].

in Figs. 14–20. They also showed almost the same characteristics for the distributions of mesh points and flow variables. The mesh adaptation procedures of both methods are concisely compared in Fig. 28. The adjoint-based method requires several costly procedures such as the adjoint analysis, an extra fine mesh generation, the interpolation of flow/adjoint variables from the coarse (present) mesh to the extra fine mesh, and one-step CFD computations on the extra fine mesh. Therefore, it is obvious that the entropy drag-based method has a simpler procedure and can be executed with lower computational cost. Thus, the newly developed entropy drag-based refinement is promising for the adaptive mesh refinement to predict drag and physical phenomena accurately.

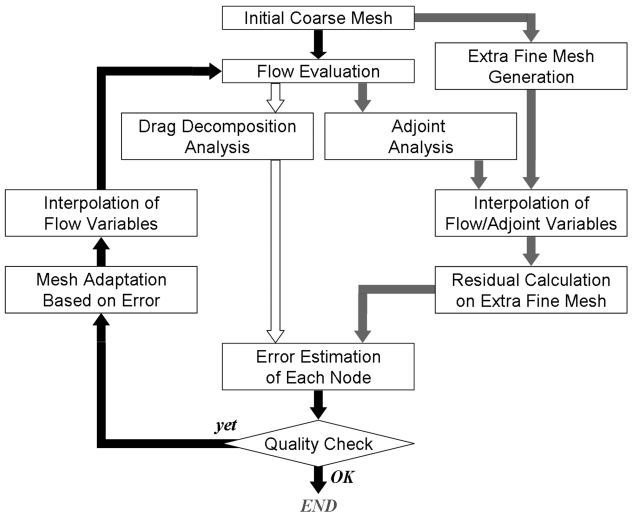

Fig. 28 Comparison of the AMR procedures of both methods. Black arrows: common process; white arrows: entropy drag based; gray arrows: adjoint based.

VIII. Conclusions

In this research, a new adaptive mesh refinement strategy has been proposed and investigated to predict drag/physical phenomena accurately and to reduce the unstructured mesh dependency efficiently. The new indicator for the adaptive mesh refinement was proposed based on the drag decomposition method which had the ability to predict the local (spurious) entropy drag amount. The entropy drag distribution was considered as one of the most effective indicators to evaluate the computational mesh quality.

The newly developed mesh refinement method was applied to inviscid transonic computations on the ONERA M6 wing, and compared with the uniform and feature-based refinements. The entropy drag-based refinement method showed a better performance than other methods, and the mesh dependency could be reduced efficiently. The entropy drag-based method was superior, not only in predicting drag accurately, but also in capturing the physical phenomena precisely. The importance of the far-field mesh resolution, in other words, the importance of the control of the mesh size transition rate from the near field to the far field, was then confirmed for accurate drag prediction. Moreover, the refinement meshes by the entropy drag-based method had almost the same characteristics as those obtained from the state-of-the-art adjoint-based method. Therefore, the newly developed entropy drag-based refinement method is promising because the indicator can be computed with lower computational cost.

For further extension of the present method, the application to viscous flow problems should be conducted. The obedient extension of the proposed method can be effective sufficiently for viscous problems. In some cases, more effective adaptive mesh refinement in viscous problems may be achieved with the special treatments for boundary layers such as the masking of the profile region.

Acknowledgments

This research was supported by a grant from the Japan Society for the Promotion of Science. The present computation was executed by using the NEC SX-7 of the Information Synergy Center at Tohoku University. The authors would like to thank Kazuhiro Kusunose for his helpful advice. The authors also would like to thank Dimitri Mavriplis for providing the unstructured hybrid meshes of DLR-F6 geometry.

References

[1] Hemsch, M. J., and Morrison, J. H., "Statistical Analysis of CFD Solutions from 2nd Drag Prediction Workshop," AIAA Paper 2004-0556, 2004.

[2] Brodersen, O., Rakowitz, M., Amant, S., Larrieu, P., Destarac, D., and Sutcliffe, M., "Airbus, ONERA, and DLR Results from the 2nd AIAA Drag Prediction Workshop," AIAA Paper 2004-0391, 2004.

[3] Laflin, K. R., "AIAA CFD Drag Prediction Workshop: An Overview," *Proceedings of the 25th ICAS Congress*, International Council of the Aeronautical Sciences, 2006.

[4] Müller, J. D., and Giles, M. B., "Solution Adaptive Mesh Refinement Using Adjoint Error Analysis," AIAA Paper 2001-2550, 2001.

[5] Kim, H. J., Takano, Y., and Nakahashi, K., "Error Estimation and Grid Adaptation Using Euler Adjoint Method," AIAA Paper 2005-5336, 2005.

[6] Kim, H. J., and Nakahashi, K., "Output-Based Error Estimation and Adaptive Mesh Refinement Using Viscous Adjoint Method," AIAA Paper 2006-1395, 2006.

[7] Balasubramanian, R., and Newman, J. C., "Comparison of Adjoint-Based and Feature-Based Grid Adaptation for Functional Outputs," AIAA Paper 2006-3314, 2006.

[8] Kusunose, K., "A Wake Integration Method for Airplane Drag Prediction," *The 21st Century COE Program International COE of Flow Dynamics Lecture Series*, Vol. 3, Tohoku University Press, Sendai, 2005.

[9] Van Der Vooren, J., and Destarac, D., "Drag/Thrust Analysis of Jet-Propelled Transonic Transport Aircraft: Definition of Physical Drag Components," *Aerospace Science and Technology*, Vol. 8, No. 6, 2004, pp. 545–556. doi:10.1016/j.ast.2004.03.004

[10] Schmitt, V., and Destarac, D., "Recent Progress in Drag Prediction and Reduction for Civil Transport Aircraft at ONERA," AIAA Paper 98-0137, 1998.

[11] Paparone, L., and Tognaccini, R., "Computational Fluid Dynamics-Based Drag Prediction and Decomposition," *AIAA Journal*, Vol. 41, No. 9, 2003, pp. 1647–1657.

[12] Yamazaki, W., Matsushima, K., and Nakahashi, K., "Unstructured Mesh Drag Prediction Based on Drag Decomposition," ECCOMAS CFD 2006, 2006.

[13] Lovely, D., and Haimes, R., "Shock Detection from Computational Fluid Dynamics Results," AIAA Paper 99-3285, 1999.

[14] Nakahashi, K., Ito, Y., and Togashi, F., "Some Challenges of Realistic Flow Simulations by Unstructured Grid CFD," *International Journal for Numerical Methods in Fluids*, Vol. 43, Nos. 6–7, 2003, pp. 769–783.
doi:10.1002/fld.559

[15] Obayashi, S., and Guruswamy, G. P., "Convergence Acceleration of a Navier-Stokes Solver for Efficient Static Aeroelastic Computations," *AIAA Journal*, Vol. 33, No. 6, 1995, pp. 1134–1141.

[16] Venkatakrishnan, V., "On the Accuracy of Limiters and Convergence to Steady State Solutions," AIAA Paper 93-0880, 1993.

[17] Sharov, D., and Nakahashi, K., "Reordering of Hybrid Unstructured Grids for Lower- Upper Symmetric Gauss-Seidel Computations," *AIAA Journal*, Vol. 36, No. 3, 1998, pp. 484–486.

[18] Spalart, P. R., and Allmaras, S. R., "A One-Equation Turbulence Model for Aerodynamic Flows," AIAA Paper 92-0439, 1992.

[19] Rivara, M. C., "Selective Refinement/Derefinement Algorithms for Sequences of Nested Triangulations," *International Journal for Numerical Methods in Engineering*, Vol. 28, No. 12, 1989, pp. 2889–2906.
doi:10.1002/nme.1620281212

[20] Sharov, D., and Fujii, K., "Three-Dimensional Adaptive Bisection of Unstructured Grids for Transient Compressible Flow Computations," AIAA Paper 95-1708, 1995.

[21] Murayama, M., Nakahashi, K., and Sawada, K., "Simulation of Vortex Breakdown Using Adaptive Grid Refinement with Vortex-Center Identification," *AIAA Journal*, Vol. 39, No. 7, 2001, pp. 1305–1312.

[22] Löhner, R., "Regridding Surface Triangulations," *Journal of Computational Physics*, Vol. 126, No. 1, 1996, pp. 1–10.
doi:10.1006/jcph.1996.0115

[23] Ito, Y., and Nakahashi, K., "Surface Triangulation for Polygonal Models Based on CAD Data," *International Journal for Numerical Methods in Fluids*, Vol. 39, No. 1, 2002, pp. 75–96.
doi:10.1002/fld.281

[24] Ito, Y., and Nakahashi, K., "Direct Surface Triangulation Using Stereolithography Data," *AIAA Journal*, Vol. 40, No. 3, 2002, pp. 490–496.

[25] Sharov, D., and Nakahashi, K., "Hybrid Prismatic/Tetrahedral Grid Generation for Viscous Flow Applications," *AIAA Journal*, Vol. 36, No. 2, 1998, pp. 157–162.

[26] Lee-Rausch, E. M., Frink, N. T., Mavriplis, D. J., Rausch, R. D., and Milholen, W. E., "Transonic Drag Prediction on a DLR-F6 Transport Configuration Using Unstructured Grid Solvers," AIAA Paper 2004-0554, 2005.

[27] Marcum, D. L., and Weatherill, N. P., "Aerospace Applications of Solution Adaptive Finite Element Analysis," *Computer Aided Geometric Design*, Vol. 12, No. 7, 1995, pp. 709–731.
doi:10.1016/0167-8396(95)00014-W

[28] Van Dam, C. P., "Recent Experience with Different Methods of Drag Prediction," *Progress in Aerospace Sciences*, Vol. 35, No. 8, 1999, pp. 751–798.
doi:10.1016/S0376-0421(99)00009-3